

Type-printable photodetector arrays for multichannel meta-infrared imaging

Junxiong Guo^{1,2,#,*}, Shuyi Gu^{1,#}, Lin Lin^{2,#}, Yu Liu^{3,4*}, Ji Cai¹, Hongyi Cai¹, Yu Tian⁵, Yuelin Zhang⁵, Qinghua Zhang⁶, Ze Liu¹, Yafei Zhang¹, Xiaosheng Zhang², Yuan Lin², Wen Huang^{2,*}, Lin Gu⁷, and Jinxing Zhang^{5,*}

¹ School of Electronic Information and Electrical Engineering, Institute of Advanced Study, Chengdu University, Chengdu 610106, China

² School of Integrated Circuit Science and Engineering, National Exemplary School of Microelectronics, University of Electronic Science and Technology of China, Chengdu 610054, China

³ School of Integrated Circuits, Tsinghua University, Beijing 100084, China

⁴ The College of Integrated Circuit Science and Engineering, National and Local Joint Engineering Laboratory for RF Integration and Micro-Packing Technologies, Nanjing University of Posts and Telecommunications, Nanjing 210023, China

⁵ Department of Physics, Beijing Normal University, Beijing 100875, China

⁶ Institute of Physics, Chinese Academy of Science, Beijing National Laboratory of Condensed Matter Physics, Beijing 100190, China

⁷ School of Materials Science and Engineering, Tsinghua University, Beijing 100084, China

These authors contributed equally: Junxiong Guo, Shuyi Gu, and Lin Lin

* Corresponding authors

E-mail addresses: guojunxiong@cdu.edu.cn (J.X. Guo), y-liu-17@tsinghua.org.cn (Y. Liu), uestchw@uestc.edu.cn (W. Huang), and jxzhang@bnu.edu.cn (J.X. Zhang)

Abstract

Multichannel meta-imaging, inspired by the parallel-processing capability of neuromorphic computing, offers significant advancements in resolution enhancement and edge discrimination in imaging systems, extending even into the mid- to far-infrared spectrum. Currently typical multichannel infrared imaging systems consist of separating optical gratings or merging multi-cameras, which require complex circuit design and heavy power consumption, hindering the implementation of advanced human-eye-like imagers. Here, we present a novel approach for printable graphene plasmonic photodetector arrays driven by a ferroelectric superdomain for multichannel meta-infrared imaging with enhanced edge discrimination. The fabricated photodetectors exhibited multiple spectral responses with zero-bias operation by directly rescaling the ferroelectric superdomain instead of reconstructing the separated gratings. We also demonstrated enhanced and faster shape classification (98.1%) and edge detection (98.2%) using our multichannel infrared images compared with single-channel detectors. Our proof-of-concept photodetector arrays simplify multichannel infrared imaging systems and hold great potential for applications in efficient edge detection in human-brain-type machine vision.

Keywords: multichannel infrared imaging, meta-imaging, ferroelectric superdomain, deep learning, edge detection

Infrared imaging systems can convert infrared radiation into human-eye-recognizable pseudoviews and are used in diverse applications, including security, surveillance, environmental monitoring, industrial inspections, and medical and health diagnoses¹⁻⁴. Current advanced infrared imaging systems are typically based on focal plane array (FPA) infrared sensors and have shown great potential for target perception⁵. However, fundamental challenges remain in achieving ultra-high resolution beyond the optical diffraction limit and in bias operation with low power consumption for hardware implementation. The human visual system can excel at rapidly and accurately identifying objective features, such as color, depth, and edges, in complex environments through the parallel processing of input light signals (Fig. 1a), and has allowed for the future manufacturing of artificial vision⁶⁻⁹. Inspired by this, recent efforts have been devoted to collecting multichannel information in terms of hardware, such as heat-assisted detection and ranging (HADAR) and meta-imagers, to enhance infrared image resolution and recognition efficiency^{10, 11}. This inevitably faces common limitations in addition to separating grating or sensor components, which necessitates a complex circuit design.

Regarding the smart perception of future infrared imaging development, graphene plasmonic photodetectors have become a promising candidate for large-scale integration into optoelectronic networks, as they directly detect infrared light with a tunable spectral response and make possible multipixel read-out circuits. Previous experiments demonstrated the excitation and tuning of plasmons in patterned graphene using traditional electrostatic gating techniques, resulting in infrared light detection with a tunable and selective response¹²⁻¹⁵. However, achieving high-quality patterned graphene remains a challenge because of the inevitable edge disorder and amorphization that occur during the patterning process using standard techniques such as chemical vapor deposition (CVD) growth, lithography, and ion/chemical etching¹⁶⁻¹⁸. Although alternative approaches have shown promise for modulating surface plasmons in continuous graphene through substrate patterning or metal gratings¹⁹⁻²¹, precise spatial modulation of the charge carrier density of graphene for tunable infrared light detection has remained challenging. Furthermore, current graphene plasmonic photodetectors employing top- or back-gate layers face common limitations in terms of complex fabrication of contact electrodes and high power consumption^{16, 22, 23}.

Ferroelectric superdomains, characterized by nanoscale domains with alternating up/downward polarization arrays, have the advantage of spatially manipulating the graphene carrier density at nanoscale resolution to construct nonuniform conductivity patterns, thereby confining graphene

plasmons for enhanced infrared detection with a tunable spectral response²⁴⁻²⁶, suggesting its unique potential for nanophotonic applications. In this study, we designed a simple two-terminal zero-bias multichannel array (MCA) detector by artificially type-printing graphene carrier density using BiFeO₃ (BFO) superdomains with hundreds-nanoscale-wide stripes for a meta-infrared imaging application. Raman signal-based spatial monitoring of the carrier density indicates that non-uniform patterning of graphene conductivity can be achieved by reconfiguring the ferroelectric superdomain. When operating at zero-bias voltage and room temperature, our device array exhibited tunable transmission spectra and selective responsivity in the mid-infrared region. Importantly, we demonstrate the integration of MCA photodetectors for infrared imaging applications, showing enhanced recognition accuracy for both overall target shapes and edge detection, along with faster training and recognition speeds compared to single-channel array (SCA) detectors.

Conceptual design of multichannel meta-infrared-imaging

Conventional infrared imaging using SCA sensors (top panel of [Fig. S1, Supporting Information](#)), which uses a linear response to map the incident intensity, faces the fundamental challenge of achieving ultrahigh spatial resolution beyond the optical diffraction limit. Consequently, textureless images famously known as the “ghosting effect” are produced. Recent developments in multichannel imagers have demonstrated their ability to enhance imaging resolution. For example, the integration of different types of sensors (e.g., HADAR) allows an imaging system to mimic the parallel processing functions of the human eye. Recently, an alternative approach using multichannel meta-imagers with external angular gratings (bottom panel of [Fig. S1](#)) was developed to accelerate the machine vision. However, both have complex spatial layouts; in particular, different devices require different bias voltages to drive, which significantly hinders the goal of achieving high energy efficiency.

The scheme of the multichannel meta-infrared imaging technique using ferroelectric superdomain-printed photodetectors is illustrated in [Fig. 1b](#). Unlike the merging of diverse cameras, the pixel points of our meta-imaging were engineered to achieve a parallel multichannel using a single aperture implemented with type-printing detectors. To ensure that the photodetector can provide selective photocurrents along with a multispectral response, we optimized the plasmonic sensing layer by rescaling the geometric shape of the ferroelectric superdomain into a 6-channel-pixel at an imaging point to avoid externally separated grating layouts. This approach can recognize a curled thumb,

whereas the conventional approach using SCA detectors cannot.

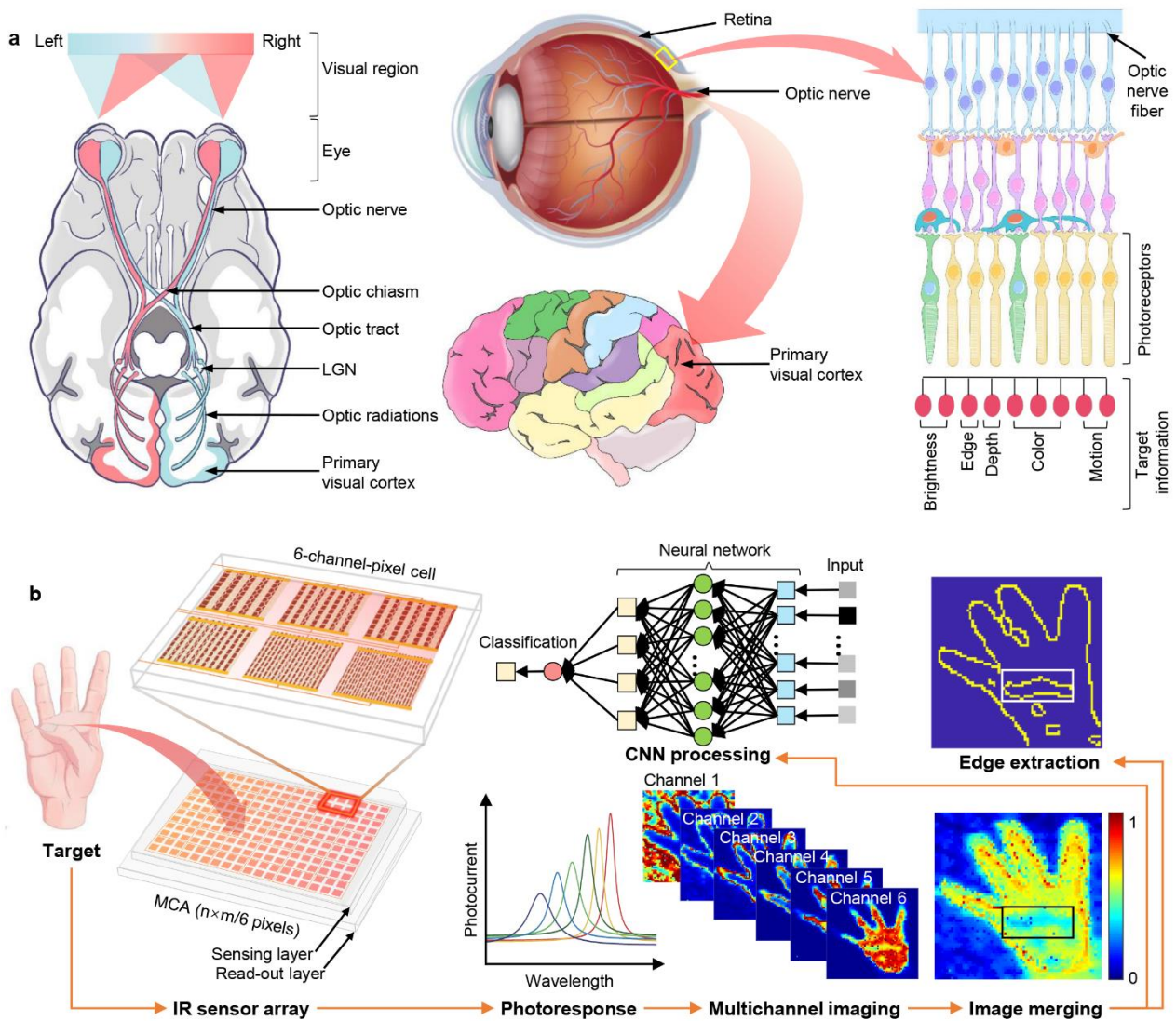


Fig. 1. Infrared imaging using type-printing multi-channel photodetector array.

(a) Illustration of the human visual system. The optical pathways are depicted in the top and lateral views in the left and middle panels, demonstrating the components of the human visual system, including the eyes, connecting pathways to the visual cortex, and other regions of the brain. The schematic diagram of the retina in the right panel highlights its remarkable ability to process various types of input light information in parallel. (b) Schematic of the meta-infrared using type-printing photodetectors. The integrated sensing layer enables selective light detection with a multi-spectral response, which avoids externally separated grating filters.

Type-printing of photodetector

As early as the Qingli period of the Song Dynasty (1041-1048 AD), China's Bi Sheng (970-1051

AD) invented the clay type, marking the birth of the movable-type printing technique. Movable printing is divided into the engraving, typesetting, and printing processes. [Figure 2a](#) illustrates the fabrication process and structure of the photodetector designed using the type-printing technique employed in this study (see [Methods](#)). Here, we used a conductive atomic force microscopy (AFM) probe (Bruker) with a platinum coating to create a ferroelectric superdomain, where the epitaxial ferroelectric BFO thin film was periodically switched to an adjacent up- and downward-striped domain array (step 1 corresponds to the engraving process of the type-printing technique). Additionally, the large-scale switching of ferroelectric superdomains was experimentally demonstrated in our previous study using a water-printing technique²⁷. The crystal structure of the BFO thin film is depicted in [Fig. S2](#), obtained using annular bright-field (ABF) high-resolution scanning transmission electron microscopy (STEM). Under the microscope, the iron atoms (depicted as yellow spheres) shifted dramatically in the upward or downward domains, indicating a reversal in the direction of ferroelectric polarization. The phase difference between the adjacent domains was 180°, as characterized by piezoelectric force microscopy (PFM) ([Fig. 2b](#)). The period of polarized strips (W , length of adjacent up- and down-ward domains) was controlled from 200 nm to 1 μm within the same BFO film. The widths of the upward and downward domains were equal within each period, that is, the width of the ferroelectric domain stripes (w) ranged from 100 to 500 nm.

Next, we transferred the CVD-grown single-layer graphene onto the BFO film (Step 2, corresponding to the printing process of the type-printing technique) using the wet transfer method²⁸. Subsequently, we employed a noncontact Raman spectroscopy monitoring technique to evaluate the doping level of graphene induced by the electrostatic effect of remnant polarization in the ferroelectric domains. The spatially resolved Raman G-band frequency shifts were used as probes for detecting the graphene carrier density²⁹. In [Fig. 2c](#), Raman G-band frequency mapping revealed periodic stripes with lower and higher frequencies, corresponding to the upward and downward domains, respectively. Additionally, Raman shift analysis ([Fig. S2](#)) showed a high 2D-to-G peak intensity ratio ($I_{2D}/I_G = 2.15$) and a low D-band intensity, confirming the high-quality and single-layer characteristics of the transferred graphene. Furthermore, comparative analysis of the Raman G-band for graphene on various BFO substrates ([Fig. S2](#)) demonstrated that the behavior of graphene on BFO with an upward domain is similar to that of a pristine BFO film, whereas the behavior differs significantly in the downward domain.

To facilitate photocurrent collection and reduce contact resistance, source/drain electrodes were

deposited on the graphene sheet (step 3). Typically, if the source/drain electrodes are made of the same metal, the device exhibits an overall zero photocurrent. In this study, we employed an asymmetric metal-doping scheme to disrupt the symmetric built-in electric field profile in the graphene channel, following a previous study on metal-graphene-metal operation at zero bias between the source and drain³⁰. Specifically, we deposited 20-nm-thick layers of palladium (Pd) and titanium (Ti) onto a graphene sheet and covered it with an 80-nm-thick layer of gold (Au) on the contact electrodes. A magnified scanning electron microscopy (SEM) image of the active region of the as-fabricated device is presented in Fig. 2d, and the raw SEM image is shown in Fig. S2.

The average Raman G-band frequency of graphene on BFO with a striped domain width of 500 nm (Figs. S2) shows that the peak position of the G-band (POG) in Raman shift for graphene on upward and downward domains were 1,586 and 1,597 cm^{-1} respectively. The periodic Raman frequency shifted from lower to higher frequencies, suggesting that graphene experienced a sharp transition from lower to higher carrier concentrations at the edges of the upward/downward domains^{19, 20}, confirming the feasibility of spatial printing of graphene carrier density without patterning of graphene sheets. Periodic patterns of graphene carrier-density modulation offer a novel approach for type-printing multiple parallel p-i junctions in a continuous graphene sheet without destroying the graphene sheet or applying complex gating electrodes (Fig. S2). Owing to the reversible and nonvolatile characteristics and nanoscale size of the ferroelectric domain, this strategy of integrating continuous graphene with a ferroelectric superdomain provides a novel approach for printing graphene carrier density into desired patterns, enabling graphene plasmonic resonance and enhancing the photocurrent in the mid- to far-infrared ranges.

To better understand our goal to achieve selective light detection beyond broadband wavelength response in the designed device, we introduced a plasmonic resonance model (Fig. 2e) in a graphene/BFO superdomain hybrid structure with electromagnetic field simulation using finite element analysis. Figure 2f illustrates the simulated cross-sections of the electric field intensity in our device, and detailed numerical simulation procedures are presented in Supplementary sections S1-S3. In this scenario, we set the chemical potential ($\mu_c = E_F$) of graphene doping by upward and downward domains with a width of 500 nm as +121 meV and -448 meV, respectively. Here, it follows the formula of $\hbar\Delta\omega = \alpha'|E_F|$ (ref. 29) as shown in Supplementary section S1, where $\hbar\Delta\omega$ and α' are the POG shift of graphene and the integral constant, respectively. The energy of the transverse-

magnetic (TM) mode is strongly confined at the graphene/ferroelectric interface with ultra-high enhanced electric field intensity. Although the energy flow enters the graphene structure on the upward ferroelectric domain, it is almost perfectly absorbed. This phenomenon might contribute to the electronic behavior near the upward and downward domains of doping graphene junctions. Importantly, for our designed plasmonic device, the resonance frequency (ω_{spr}) could be easily regulated by rescaling the ferroelectric superdomain width (d) which follows eqn. (1),

$$\omega_{\text{spr}} = \left(\frac{e^2 E_{\text{F}}}{2\pi\hbar^2 \varepsilon_0 \varepsilon_{\text{r}}} \left(q_0 \pm N \frac{\pi}{d} \right) \right)^{\frac{1}{2}} \quad (1)$$

where e , \hbar , ε_0 , ε_{r} , and q_0 represent the element charge, reduced Planck constant, vacuum dielectric constant, relative dielectric constant of BFO, free space wave vector of incident light, and $N = 1, 2, 3, \dots$, respectively. A detailed derivation of the formula is provided in [Supplementary section S4](#).

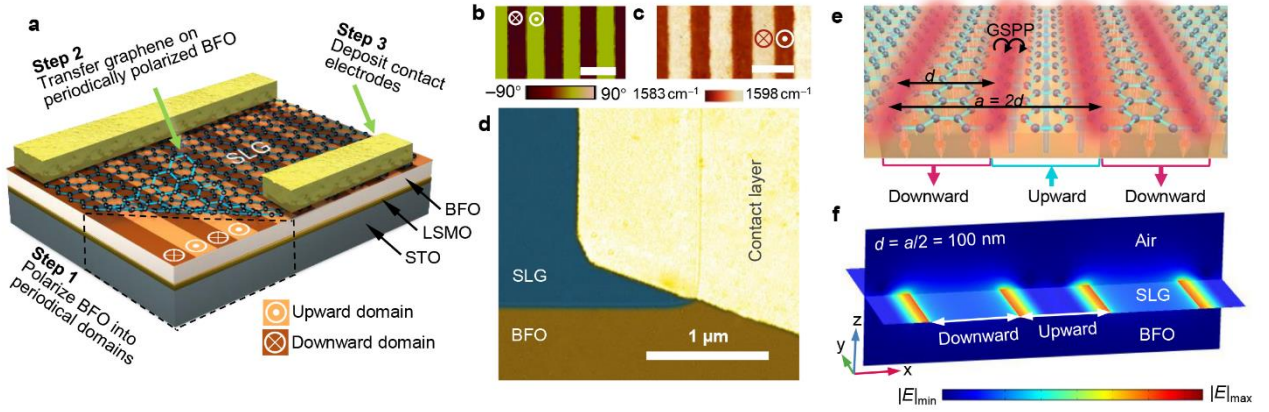


Fig. 2. Fabrication and architecture of type-printable plasmonic photodetector.

(a) Schematic of the experimental setup for printing graphene/BFO superdomain-based plasmonic photodetector. The BFO film epitaxial growth on an STO substrate with a covering LSMO ($\text{La}_x\text{Sr}_{1-x}\text{MnO}_3$) electrode layer. (b) PFM phase image of BFO superdomains, showing the periodical ribbons patterned adjacent to upward and downward domains. (c) G-band frequency mapping for graphene on BFO superdomains with a period of $1 \mu\text{m}$. (d) SEM image of the active area of the fabricated graphene/BFO device. The false color focuses on the graphene on the BFO film. (e) Schematic of the graphene plasmon resonator architecture for a plane wave normally infrared incidence. GSPP represents graphene surface plasmon polaritons. (f) Simulated electric field intensity for graphene plasmon resonator by a three-dimensional model. The excited GSPP is highly confining in the borders of upward/downward domains at the graphene/BFO interface. SLG denotes single-layer graphene.

Rescaling ferroelectric superdomain for multi-spectral response

To validate the performance of this printable architecture, we fabricated a device array on the same BFO thin film by rescaling the ferroelectric domain width (corresponding to the type-printing

process). Two types of device arrays were fabricated (Fig. S3) to facilitate the optical (sample size of 5 mm × 5 mm) and photoelectric (sample size of 10 mm × 10 mm) measurements. Each unit contained six BFO stripes with domain widths ranging from 100 to 500 nm. The optical and corresponding PFM phase images of the fabricated device array are shown in Fig. 3a. The AFM Raman images (Fig. 3b) and corresponding POG peaks (Fig. S2) strongly support our idea of type-printing desired graphene carrier patterns by resetting the ferroelectric domain width.

We then focused on the spectral response of graphene to the BFO superdomains of different widths. To achieve this, we used an AFM probe to direct incident light precisely to specific microregions. The transmission measurements are schematically illustrated in the inset of Fig. 3c, where T and T_0 correspond to the transmission values of the BFO film epitaxially grown on the SrTiO₃ (STO) substrate with and without graphene, respectively. The measured extinction spectra of the graphene/BFO hybrid structures are shown in Fig. 3c. Within the periodically printed graphene stripes on the BFO superdomains, we observed two notable features. First, a remarkably selective resonant peak appeared with domain widths ranging from 100 to 500 nm. Second, the resonant peaks shifted from low frequency (1084 cm⁻¹) to high frequency (1292 cm⁻¹) with a decreasing domain period. The coincidence between the blue-shift phenomenon and Equation (1) can be attributed to the matching of the wave vector of the incident wave in free space and the wave vector of the excited GSPP, thereby forming a resonant coupling effect.

The photocurrent of the device array was measured using an automated wavelength-tuning laser to generate incident signals that were added to the graphene sheet at a 90° angle (in the vertical direction) with a zero-bias voltage. All the photocurrents were obtained by averaging the peak values from 12 points under illumination at different wavelengths. The highest photocurrent in each cell was achieved near the resonant wavelength (Fig. S3). Additionally, we investigated the photoresponsivity using $R = I_{\text{ph}}/P_{\text{in}}$, where I_{ph} and P_{in} represent the photocurrent and incident laser power, respectively. The calculated results (Fig. S3) demonstrate that our device array exhibits a significantly selective detection factor β , which is the ratio of the highest and lowest photoresponsivity values in each cell.

We then discussed the performances of typical infrared photodetectors based on emerging materials operating at room temperature, as shown in Fig. 3d. Compared to previously reported metal plasmon-enhanced graphene photodetectors, such as metal-graphene-metal structure³⁰, the intrinsic plasmons in patterned graphene offer an incomparable advantage in the mid-infrared range. Its surface plasmons can be used to resonantly enhance the absorption for tunable photodetection controlled by

the grating effect, providing appealing spectral selectivity with ultra-high tunability¹⁵. For the photodetector demonstrated herein, it achieved an enhanced photoresponsivity of approximately 30 mA W⁻¹. While this photoresponsivity was not the highest recorded among current infrared photodetectors using emerging materials³¹, it was comparable to that of conventional graphene plasmonic devices for mid-infrared detection based on nanopatterned graphene photograting structures³¹⁻³⁴. This can be attributed to the effective plasmon excitations and perfect crystallinity of the graphene sheet, with the latter effectively reducing light scattering compared to nanopatterned graphene. Another interesting phenomenon is that the device we designed can operate at zero bias voltage, with its detection range within the IR-C band (3 μm to 1 mm, CIE 17-21-004, <https://cie.co.at/eilvterm/17-21-004>). This coincided with the biological thermal radiation, particularly the fact that over 50% of the energy emitted by the human body was concentrated in the range of 8 to 15 μm, which our device could handle. Furthermore, the convenience of printing graphene carrier-density patterns by switching ferroelectric domains at the nanoscale without the need for complex nanofabrication, as seen in conventional graphene plasmonic devices, allows for a remarkably selective response over broadband wavelengths and features a simple multi-channel array integration for light detection in the infrared region. The characteristics exhibited by our device provide a promising route for advanced multi-channel infrared imaging that combines low power consumption with high recognition capability, as mentioned earlier.

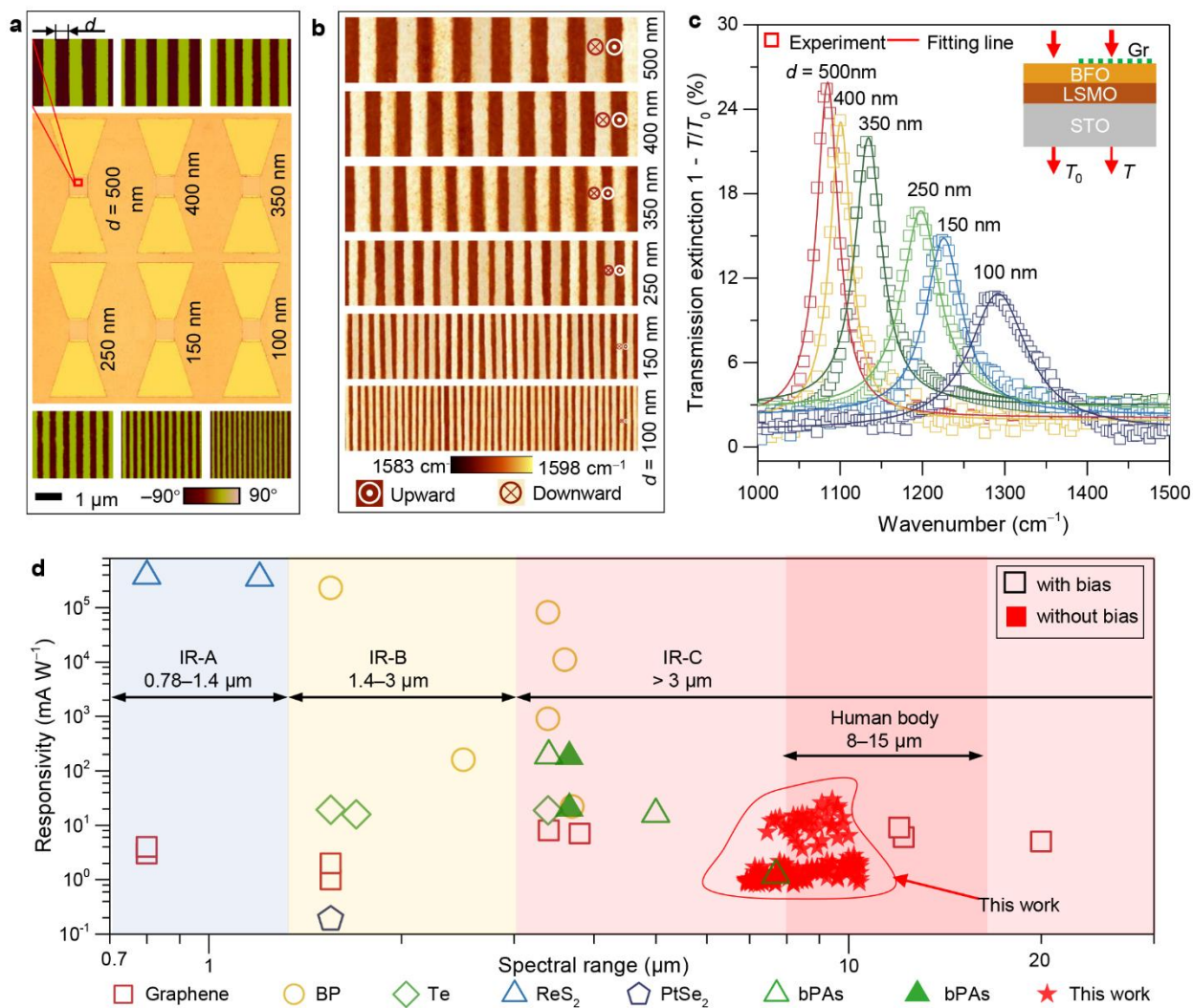


Fig. 3. Characterization of type-printing detector array.

(a) Integrating graphene photodetector array onto BFO film. The middle column is the optical image of the fabricated device array with a ferroelectric domain width ranging from 100 to 500 nm. The top and bottom columns are the PFM phase images of the corresponding BFO superdomains. (b) AFM-Raman mapping images for graphene carrier density printed by rescaling BFO superdomain. (c) Tunable transmission extinction spectra ($1 - T/T_0$) for graphene by rescaling BFO superdomain. (d) Comparison of responsivity with typical types of infrared photodetectors using metal-semiconductor-metal structure working at room temperature. The data were collected from refs. 31-34.

Multichannel infrared imaging for enhancing edge detection

To evaluate the imaging capability of the fabricated array of infrared photodetectors, we used the OPENZYNG open-source project (<https://github.com/openzynqhardware/openzynq.git>) to simulate the process. A schematic of the simulation procedure is shown in Fig. S4. For data collection, we employed a commercial Melexis infrared camera with 192×144 pixels to capture the desired temperature. The simulations have already been demonstrated for both the SCA with a ferroelectric domain width of 500 nm and MCA with ferroelectric domain widths ranging from 100 to 500 nm

(Fig. 4a and Figs. S5). We observed that MCA detectors excel at recognizing inner edge profiles such as curled fingers and overlapped leaves, whereas SCA detectors fall short in this regard. The images generated by the MCA showed a more pronounced temperature difference between the regions of the fingers and palms, indicating that the MCA can identify more complex edge features of the targets when processing images.

An off-chip learning task involving the classification of gesture images (0-5, as shown in Fig. 4a) was conducted to evaluate the learning capability of the MCA detectors in infrared imaging. The training accuracies for gesture recognition were 99.2% and 100% based on the SCA and MCA detectors, respectively, after 3,600 iterations (Fig. 4b). The MCA detectors exhibited a significantly faster training speed than the SCA detectors because of the intrinsic differences between the edge profiles. However, we analyzed the changes in classification accuracy over 100 epochs for gesture recognition, with each epoch consisting of 3,600 iterations. Figure 4c reveals two key findings. First, when dealing with a small sample size, the MCA performs better than the SCA in gesture recognition accuracy. For example, at 10 epochs, the recognition accuracies of the MCA-based- and SCA-based detectors were 96.7% and 63.7%, respectively. At 40 epochs, they reach 97.8% and 88.9%, respectively. Second, when faced with a large sample size, the difference in gesture recognition accuracies between the two methods became small. For example, at 100 epochs, the recognition accuracies of the MCA and SCA were 98.1% and 93.2%, respectively.

The second important application of MCA detectors is enhanced edge detection, which was demonstrated using an off-chip learning task involving the recognition of curled fingers. As shown in Fig. 4a, the curled finger edges extracted from the infrared images using the MCA method are much more distinct than the SCA, which failed to capture them. The same trend was observed in the images of the overlapped leaves (Fig. S5). The results of training in the presence and absence of curled fingers showed that the MCA and SCA methods had training accuracies of 76.3% and 99.8%, respectively (Fig. 4d). This difference was much larger than that of the gesture training, with the discrepancies decreasing from 0.8% to 23.5%. Similar to gesture training, the MCA detectors exhibited a significantly faster training speed than the SCA detectors for curled fingers. More importantly, during curled finger recognition, after 100 epochs, the recognition accuracy of the MCA approach reached a high level of 98.2%, whereas that of the SCA remained at approximately 69.7% (Fig. 4e). These results further demonstrate that the MCA method can significantly improve the accuracy of target recognition in infrared imaging at the hardware level, particularly by enhancing the edge detection

accuracy in complex environments.

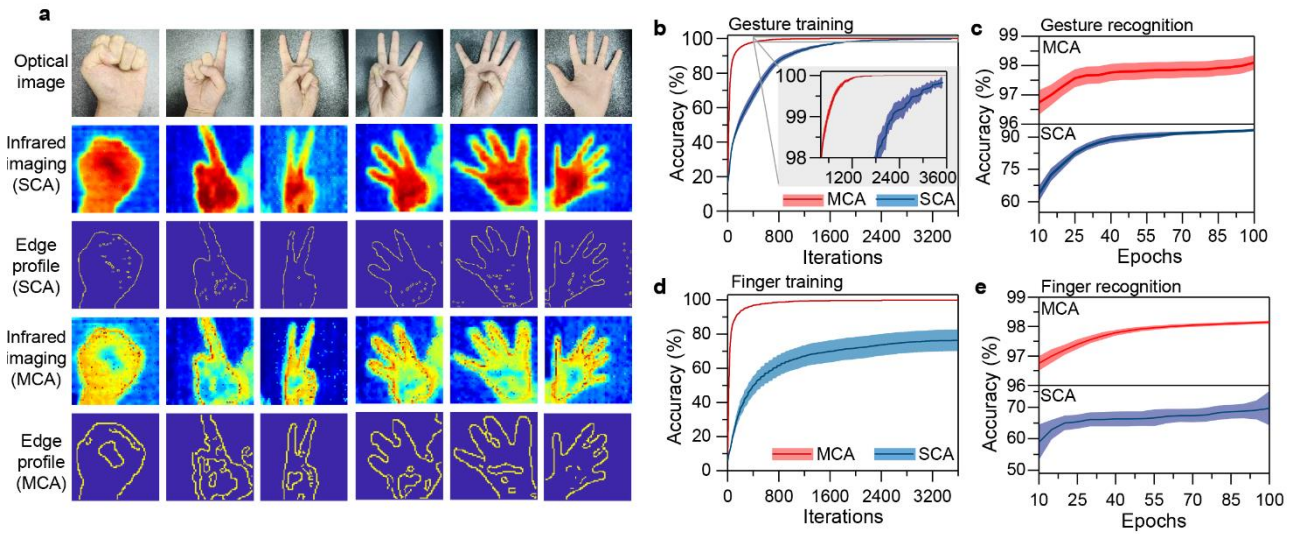


Fig. 4. Applications of type-printing detectors in gesture infrared imaging and recognition.

(a) Infrared imaging for different gestures with single- and multi-channel array of type-printing photodetectors. (b, c) Evolution of classification accuracy over 100 epochs for gesture recognition, with each epoch consisting of 1,000 iterations. (d, e) Changes in the classification accuracy over 100 epochs for curled finger recognition, with each epoch including 1,000 iterations.

Conclusions

We developed a printable photodetector array by integrating monolayer graphene with a BFO thin film that features a nanoscale-wide stripe superdomain and demonstrated that this type of device array is designed for multichannel meta-infrared imaging applications and offers significant enhancement of edge detection. Graphene was monitored non-contactfully for dopants using Raman shifts, and doping patterns on ferroelectric superdomains were observed at the nanoscale. The printable photodetectors operated at a zero-bias voltage and exhibited a high photoresponsivity of approximately 30 mA W^{-1} at room temperature. This can be attributed to the resonant coupling of graphene plasmons with incident light. Moreover, the device arrays exhibited a selective response in the mid-infrared region through direct rescaling of the BFO superdomain width under ambient conditions. This work demonstrates the precise spatial control of graphene carrier density by reversing the ferroelectric domains at the nanoscale. The excellent compatibility of graphene sheets with different substrates offers several advantages over conventional devices that rely on complex nanofabrication techniques. Additionally, we proved that multichannel array detectors can enhance

shape and edge detection in infrared imaging. These features allow for future integrated optoelectronic platforms with simple circuit designs and low power consumption.

Methods

BFO film epitaxial growth. BFO thin films were epitaxially grown on (001)-oriented STO substrates with LSMO as the bottom electrode using pulsed laser deposition. For the deposition of both LSMO and BFO films, a KrF excimer laser, with 248 nm wavelength, 5 Hz repetition rate, and $\sim 1.5 \text{ J cm}^{-2}$ energy density, was employed. The films were grown in an atmosphere of 0.2 mbar oxygen pressure at 700 °C. The thicknesses of the films were maintained at approximately 25 nm.

Device fabrication. For ferroelectric polarization switching, the upward and downward domains were switched by scanning the surface with a nanotip under a +12 V (−12 V) bias exceeding the coercive voltage (Fig. 2a, step 1). For the convenience of guiding the incident light to specific areas and fixing the active illuminating regions, the BFO film was patterned into an array with a fixed area, and the etched depth was controlled at approximately 10 nm in each unit using reactive ion etching (RIE) before polarization.

Single-layer graphene was transferred onto a BFO film using an improved wet method²⁸ (Fig. 2a, step 2). Briefly, the polymethyl methacrylate (PMMA, Aladdin) solution (20 mg mL^{-1}) was spin-coated on CVD-grown monolayer graphene/copper foils (SixCarbon Technology Shenzhen) at 3,000 rpm for 30 s and dried at 120 °C for 90 s in air. Ammonium persulfate (0.1 M) was used to etch the copper substrate, and the PMMA/graphene film was washed several times with deionized water to remove the etchant residue. The prepolarized BFO film was then placed in water at a tilting angle underneath the PMMA/graphene film to support it. After drying in air, the PMMA was removed with an acetone bath at 50 °C and washed with ethanol. The monolayer graphene was etched to the same area as the marked BFO using oxygen plasmons. Subsequently, the Au/Ti and Au/Ni source and drain electrodes were deposited on the border of the graphene to fabricate the device (Fig. 2a, step 3). The thicknesses of the Au layer and Ti and Pd layers were 80 and 20 nm, respectively.

Measurements. PFM experiments were performed under ambient conditions at room temperature using an Infinity Asylum Research AFM instrument. The crystal structures of BFO were determined using TEM (JEOL 2100F) operated at 200 keV and equipped with a probe aberration corrector (CEOS) and double spherical aberration (Cs) correctors. The spatial resolution of the

microscope reached 90 pm at an incident semiangle of 20 mrad. Subsequently, a fast Fourier transform multislice approach was used for the STEM configuration. Raman-AFM mapping images and the corresponding spectral data in the same region were acquired using a fully integrated system based on the Smart SPM state-of-the-art scanning probe microscope and XploRA Raman microspectrometer (HORIBA). In all cases, 532 nm laser excitation and tip-enhanced Raman spectroscopic resolution were used. The transmission spectra were collected using a Spotlight 200i FT-IR Microscopy System (PerkinElmer Inc.) with a spot resolution better than 10 μm . The photocurrents were performed using a Keithley 4200A-SCS Parameter Analyzer (Tektronix), and the incident source was produced by a tunable laser (EKSPLA, 2.3–10 μm), at zero bias voltage between the contact electrodes. The laser intensities, including the Raman and electrical measurements, were set below 1 mW to avoid artifacts caused by laser-induced heating. All measurements were performed in ambient air at room temperature.

Numerical simulations. The electrical properties of graphene were calculated using random phase approximation (RPA), and the dynamic optical response of graphene was derived from the Kubo formula ([Supplementary Section S2](#)) (ref. 35, 36). Electromagnetic field simulation was performed using the finite element method ([Supplementary Section S3](#)). Infrared imaging simulations were performed using an open-resource project, and the details are shown in [Supplementary Section S5](#).

Acknowledgments

The authors thank Ms. Xiaoxu Lai and Prof. Ronghui Guo from Sichuan University for their support with the Raman mapping and photocurrent measurements. We also thank Dr. Prof. Lei Bi from the University of Electronic Science and Technology of China for discussions on spectral response. This work was financially supported by the National Natural Science Foundation of China (Grant Nos. 62371095, 62201096, and 62074029), National Key Research and Development Program of China (Grant No. 2022YFB3206100), Key R&D Program of Sichuan Province (Grant Nos. 2022ZHCG0041, 2022JD TD0020, and 2022YFG0163), Natural Science Foundation of Sichuan Province (Grant Nos. 24NSFSC0409 and 2022NSFSC0652), and Aeronautical Science Foundation (Grant No. 20200024080001).

Author contributions

J. G., Y. L., W. H., and J. Z. conceived and designed the experiments. Y.T., Y.Z., and J.Z. provided the epitaxially grown BFO films. Y.T. and Y.Z. wrote the ferroelectric superdomain using a type-printing technique and characterized the PFM images. J. G., Y. L., and L. L. fabricated the devices. Q. Z. and L. G. conducted high-resolution TEM characterization. L. L. conducted SEM characterization. J. G. and L. L. conducted the Raman characterization and optical transmission measurements. J. G. and L. L. conducted the photodetection experiments. J. G., Y. L., L. L., J. C., Z. L., and Y. Z. performed the theoretical models and calculations for the electromagnetic field simulations. J. G., S. G., Y. L., and H. C. designed and performed the infrared imaging and deep learning. J. G., Y. L., X. Z., Yuan. L., W. H., and J. Z. analyzed the data. J. G., Y. L., W. H., and J. Z. supervised the experiments. J. G. and Y. L. wrote the paper and Supporting Information. All authors participated in the data analysis and discussion of this work.

Competing interests

The authors declare no competing interests.

Data availability

Data supporting the findings of this study are available from the corresponding authors upon request.

Additional information

Supporting information

Supplementary sections S1-S6 and Figs. S1-S5.

References

1. Ding Y.C., *et al.* Uncooled self-powered hemispherical biomimetic pit organ for mid- to long-infrared imaging. *Sci Adv.* **8**, eaba8432 (2022).
2. Zhao Y., *et al.* High-speed scanless entire bandwidth mid-infrared chemical imaging. *Nat Commun.* **14**, 3929 (2023).
3. He H.J., *et al.* Mapping enzyme activity in living systems by real-time mid-infrared photothermal imaging of nitrile chameleons. *Nat Methods.* <https://doi.org/10.1038/s41592-41023-02137-x> (2024).
4. Rodrigo D., *et al.* Mid-infrared plasmonic biosensing with graphene. *Science.* **349**, 165-168 (2015).
5. Martyniuk P., *et al.* New concepts in infrared photodetector designs. *Applied Physics Reviews.* **1**, (2014).
6. Mennel L., *et al.* Ultrafast machine vision with 2D material neural network image sensors. *Nature.* **579**, 62-66 (2020).
7. Jordan M.I., Mitchell T.M. Machine learning: Trends, perspectives, and prospects. *Science.* **349**, 255-260 (2015).
8. Hippalgaonkar K., *et al.* Knowledge-integrated machine learning for materials: lessons from gameplaying and robotics. *Nat Rev Mater.* **8**, 241-260 (2023).
9. Rahwan I., *et al.* Machine behaviour. *Nature.* **568**, 477-486 (2019).
10. Bao F., *et al.* Heat-assisted detection and ranging. *Nature.* **619**, 743-748 (2023).
11. Zheng H., *et al.* Multichannel meta-imagers for accelerating machine vision. *Nat Nanotechnol.*

<http://dx.doi.org/10.1038/s41565-41023-01557-41562> (2024).

12. Freitag M., *et al.* Photocurrent in graphene harnessed by tunable intrinsic plasmons. *Nat Commun.* **4**, 1951 (2013).
13. Yan H., *et al.* Damping pathways of mid-infrared plasmons in graphene nanostructures. *Nat Photonics.* **7**, 394 (2013).
14. Yan H., *et al.* Tunable infrared plasmonic devices using graphene/insulator stacks. *Nat Nanotechnol.* **7**, 330-334 (2012).
15. Guo Q., *et al.* Efficient electrical detection of mid-infrared graphene plasmons at room temperature. *Nat Mater.* **17**, 986 (2018).
16. Low T., Avouris P. Graphene plasmonics for terahertz to mid-infrared applications. *ACS Nano.* **8**, 1086-1101 (2014).
17. Novoselov K.S., *et al.* A roadmap for graphene. *Nature.* **490**, 192-200 (2012).
18. Ferrari A.C., *et al.* Science and technology roadmap for graphene, related two-dimensional crystals, and hybrid systems. *Nanoscale.* **7**, 4598-4810 (2015).
19. Echtermeyer T.J., *et al.* Strong plasmonic enhancement of photovoltage in graphene. *Nat Commun.* **2**, 458 (2011).
20. Fang Z.Y., *et al.* Plasmon-induced doping of graphene. *ACS Nano.* **6**, 10222-10228 (2012).
21. Poumirol J.-M., *et al.* Electrically controlled terahertz magneto-optical phenomena in continuous and patterned graphene. *Nat Commun.* **8**, 14626 (2017).
22. Koppens F.H., *et al.* Photodetectors based on graphene, other two-dimensional materials and hybrid systems. *Nat Nanotechnol.* **9**, 780-793 (2014).
23. Long M., *et al.* Progress, challenges, and opportunities for 2D material based photodetectors. *Adv Funct Mater.* **29**, 1803807 (2019).
24. Spaldin N.A., Ramesh R. Advances in magnetoelectric multiferroics. *Nat Mater.* **18**, 203-212 (2019).
25. Baek S.H., *et al.* Ferroelastic switching for nanoscale non-volatile magnetoelectric devices. *Nat Mater.* **9**, 309-314 (2010).
26. Langenberg E., *et al.* Strain-engineered ferroelastic structures in PbTiO₃ Films and their control by electric fields. *ACS Appl Mater Inter.* **12**, 20691-20703 (2020).
27. Tian Y., *et al.* Water printing of ferroelectric polarization. *Nat Commun.* **9**, 3809 (2018).
28. Suk J.W., *et al.* Transfer of CVD-grown monolayer graphene onto arbitrary substrates. *ACS Nano.* **5**, 6916-6924 (2011).
29. Pisana S., *et al.* Breakdown of the adiabatic Born-Oppenheimer approximation in graphene. *Nat Mater.* **6**, 198-201 (2007).
30. Mueller T., *et al.* Graphene photodetectors for high-speed optical communications. *Nat Photonics.* **4**, 297-301 (2010).
31. Liu C., *et al.* Silicon/2D-material photodetectors: from near-infrared to mid-infrared. *Light Sci Appl.* **10**, 123 (2021).
32. Goldstein J., *et al.* Waveguide-integrated mid-infrared photodetection using graphene on a scalable chalcogenide glass platform. *Nat Commun.* **13**, 3915 (2022).
33. Liu W., *et al.* Graphene charge-injection photodetectors. *Nat Electron.* **5**, 281-288 (2022).
34. Guo Q., *et al.* Efficient electrical detection of mid-infrared graphene plasmons at room temperature. *Nat Mater.* **17**, 986-992 (2018).
35. Hwang E., *et al.* Carrier transport in two-dimensional graphene layers. *Phys Rev Lett.* **98**, 186806 (2007).
36. Stauber T. Plasmonics in Dirac systems: from graphene to topological insulators. *J Phys-Condens Mat.* **26**, 123201 (2014).